Article

Earth shaped by primordial H_2 atmospheres

https://doi.org/10.1038/s41586-023-05823-0

Received: 27 July 2022

Accepted: 10 February 2023

Published online: 12 April 2023

Check for updates

Edward D. Young[1]✉, Anat Shahar[2] & Hilke E. Schlichting[1]

Earth's water, intrinsic oxidation state and metal core density are fundamental chemical features of our planet. Studies of exoplanets provide a useful context for elucidating the source of these chemical traits. Planet formation and evolution models demonstrate that rocky exoplanets commonly formed with hydrogen-rich envelopes that were lost over time[1]. These findings suggest that Earth may also have formed from bodies with hydrogen-rich primary atmospheres. Here we use a self-consistent thermodynamic model to show that Earth's water, core density and overall oxidation state can all be sourced to equilibrium between hydrogen-rich primary atmospheres and underlying magma oceans in its progenitor planetary embryos. Water is produced from dry starting materials resembling enstatite chondrites as oxygen from magma oceans reacts with hydrogen. Hydrogen derived from the atmosphere enters the magma ocean and eventually the metal core at equilibrium, causing metal density deficits matching that of Earth. Oxidation of the silicate rocks from solar-like to Earth-like oxygen fugacities also ensues as silicon, along with hydrogen and oxygen, alloys with iron in the cores. Reaction with hydrogen atmospheres and metal–silicate equilibrium thus provides a simple explanation for fundamental features of Earth's geochemistry that is consistent with rocky planet formation across the Galaxy.

Models for the accretion of the Earth date back decades[2]. Modern versions often focus on matching Earth's chemical features by ascribing different chemical characteristics to possible planetary embryos and planetesimals in *N*-body simulations of the accretion process. To match Earth's chemistry, gradients in parameters such as water availability and oxygen fugacity across the protoplanetary disk are invoked along with prescriptions for partial equilibration during discrete collision events[3]. These models by necessity involve a large number of adjustable parameters, thus permitting reasonable fits. The models are logically sound, but their veracity is less clear. Here we present an alternative approach that accounts for recent insights gained from rocky exoplanet formation and the important role of primary atmospheres, and use this to re-examine Earth's formation.

Two properties of the inner Solar System would seem to have worked against the formation of a water-rich, oxidized (relative to a solar gas) planet like the Earth: (1) the material in the vicinity of 1 AU from our star was probably dry[4], and (2) this material was relatively reduced (that is, not oxidized)[5]. These conclusions are based on the emerging view that the best samplings of inner Solar System rocks, apart from Earth itself, are enstatite chondrites (E chondrites) and their igneous equivalents (aubrites)[6]. E chondrites closely resemble the Earth in at least 15 isotopic systems[7] and, unlike other meteorite groups, have sufficient metal to explain the mass fraction of Earth's core[8]. Furthermore, the inner Solar System is bound, spatially, by E-chondrite-like material. The inner edge is demarcated by Mercury, which is compositionally similar to E chondrites and aubrites[9]. The outer edge is marked by the inner-most asteroid belt, where E-type asteroids are most abundant; E-type and some M-type asteroids are likely sources for E-clan meteorites[10,11]. This further suggests that the inner Solar System was mainly, although not entirely[12], dry and reducing much like E-clan meteorites. Enstatite chondrites themselves may represent olivine-poor vestiges of Earth's building blocks[6].

Recent exoplanet observations have revealed that the most common planets in our Galaxy discovered so far are larger than Earth and smaller than Neptune[13], and comprise two distinct groups. One group is composed of rocky planets with hydrogen (H_2)-rich envelopes that make up a few per cent of their total mass, the so-called sub-Neptunes. The other includes rocky planets absent in H_2-rich atmospheres, the so-called super-Earths[14]. These two populations are divided by a 'radius valley' in planet size near 1.5 $R_\oplus$ to 2.0 $R_\oplus$ (ref. [15]). Planet formation and evolution models to explain the radius valley have demonstrated that the rocky super-Earths we observe today probably formed with H_2-rich envelopes that were lost over time[16] (in about 10^8 yr to 10^9 yr) by either photo-evaporation and/or core-powered mass loss, suggesting that the super-Earths and sub-Neptunes originally formed as one population with H_2 atmospheres[17,18]. Through the studies of these exoplanets, we have gained a greater appreciation for the ubiquity of H_2-rich atmospheres accreted from protoplanetary disks during the first several million years of planetary growth[19]. Our calculations illustrate how this process may have shaped Earth's chemistry and that Earth's formation can be successfully placed into the context of rocky exoplanet formation within our Galaxy.

Although decay of the short-lived radionuclide ^{26}Al dominated the thermal structure of small planetesimals formed early in the Solar System, the thermal histories of more massive bodies (greater than about 0.05 $M_\oplus$) were controlled by the conversion of gravitational potential energy into heat during accretion. As a result, planetary embryos in the early Solar System were initially molten. Upon cooling

[1]Department of Earth, Planetary, and Space Sciences, University of California Los Angeles, Los Angeles, CA, USA. [2]Carnegie Institution for Science, Earth and Planets Laboratory, Washington, DC, USA. ✉e-mail: eyoung@epss.ucla.edu

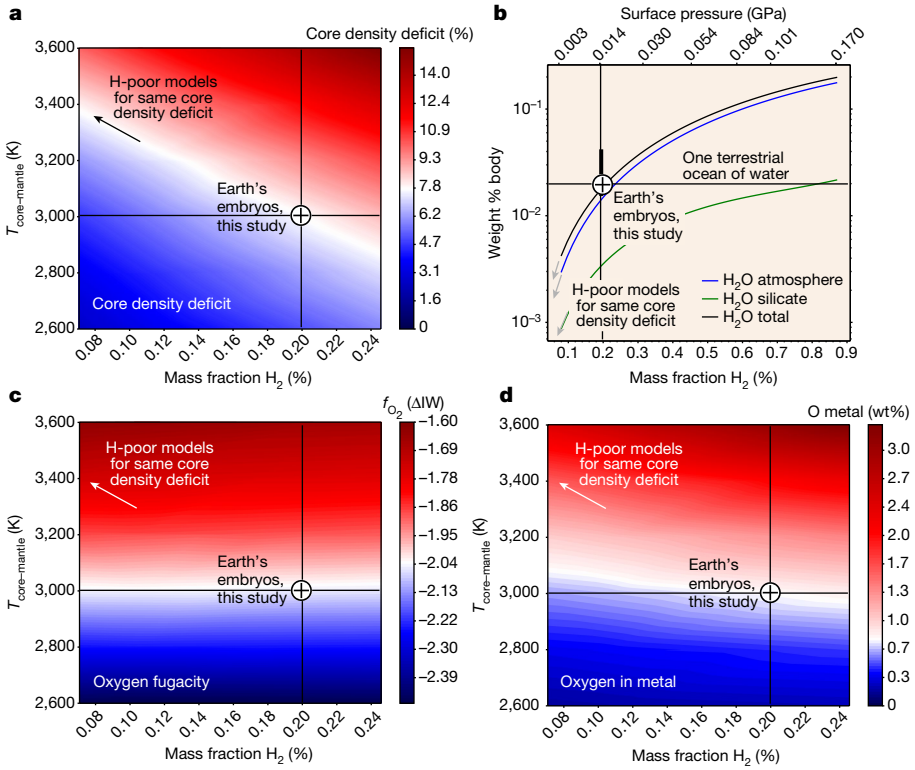

Fig. 1 | Summary of thermodynamic calculations. The calculations show that Earth's core density deficit, mass fraction of water and oxygen fugacity can be explained in a self-consistent way with a global equilibrium model that includes an H_2-rich primary atmosphere, a silicate magma ocean and a metal core. The results are shown for 0.5-$M_\oplus$ embryos as a function of metal–silicate equilibration temperature ($T_{core-mantle}$) and the initial mass fraction of primary H_2-rich atmospheres. In each panel, parameters for embryos that would fit the Earth at $T_{core-mantle}$ = 3,000 K (see text) are shown by a circle with a cross symbol. The target values for Earth are shown in the white regions in the contour plots. **a**, Density deficits in metal cores with a target value of about 8% by weight (see text). **b**, H_2O mass fraction for the embryos where $T_{core-mantle}$ = 3,000 K showing that the model satisfying Earth's core density deficit (**a**) results in one terrestrial ocean worth of H_2O (circle with a cross). Here the pressures at the base of the atmosphere after equilibration are shown on the upper abscissa, with the best fit for Earth's antecedent embryos corresponding to pressures at the surface of the magma ocean of about 0.014 GPa (140 bar). **c**, The intrinsic O_2 fugacities (f_{O_2}) relative to the iron-wüstite reference, illustrating that the same model that matches Earth's core density yields Earth's intrinsic f_{O_2} of about ΔIW − 2.1. **d**, The weight per cent of O in metal as predicted by this model. The arrow in **a** points to the direction of models that satisfy Earth's core density deficit but where H is scarce or absent. This same trajectory is illustrated in **b**–**d**.

to below the threshold surface temperature for thermal escape of gas molecules, the embryos are expected to have accreted gas from the surrounding protoplanetary disk, thus acquiring H_2-rich primary atmospheres. Once an optically thick envelope has been accreted, subsequent cooling of the embryo–atmosphere system occurs through the top of the atmosphere at the radiative–convective boundary[19]. The cooling is slowed relative to radiation from the surface of the magma ocean by the factor $(T_e^4/\tau)/T_s^4$, where T_e is the equilibrium temperature, τ is the Rosseland mean optical depth at the radiative–convective boundary and T_s is the surface temperature of the magma ocean[19]. For the relevant optical depths at the radiative–convective boundary of atmospheres considered here (for example, $\tau \approx 100$) and equilibrium temperatures similar to Earth's, cooling is slower by a factor of about 10^6 relative to the no-atmosphere case, resulting in magma oceans below the atmospheres that persist for tens of millions of years.

If material and chemical exchange is efficient, chemical equilibrium between the magma oceans and the atmospheres will occur[20]. Convective velocities in the magma ocean are the limiting factor for the rate of exchange. Scaling laws based on experiments indicate that convection in magma oceans the size of the embryos leads to linear velocities of the order of 1 m s^{-1} for surface temperatures above the solidus[21,22]. The effect of the optically thick atmosphere is to decrease the radiative flux and thus slow the convective velocity by the factor $((T_e^4/\tau)/T_s^4)^{1/3} \approx 100$. The resulting convective turnover times of the order of 10^4 years are still more than sufficient to allow equilibrium between the magma oceans and the overlying atmospheres over the approximately 10^7-year cooling timescales of the magma ocean–atmosphere system.

Ingress of protoplanetary disk gas (solar gas) into Earth's building blocks is evidenced by noble gas isotope ratios from mantle rocks[23–27]. Conversely, it appears that Mars has no vestiges of solar gas in its interior[28,29]. As gas is soluble in molten rock but not solid rock, the lack of solar gas in the interior of Mars is to be expected. Isotopic constraints as well as the similarity of its mass to the so-called isolation mass for a minimum-mass solar nebula suggest that Mars is a planetary embryo that grew within about 2 Myr to 4 Myr and probably had a magma ocean[30]. However, Mars was insufficiently massive to retain an H_2-rich atmosphere at surface temperatures consistent with molten rock, thus precluding exchange between the atmosphere and the interior (Methods). Comparing the gravitational binding energy to the thermal energy of H_2 gas molecules implies that a body the mass of Mars, 0.1 $M_\oplus$, can only accrete a primary H_2-dominated atmosphere from the disk after its surface cooled to ≤700 K, well below the solidus for rock (Extended Data Fig. 1)[19]. Therefore, one would expect that a magma ocean would not have been exposed to the primary atmosphere in the case of Mars, consistent with isotopic constraints.

Not all planetary embryos that grew in the presence of the protoplanetary disk need have been the mass of Mars, however. Surface densities greater than that of the minimum-mass solar nebula, radial drift of disk material[31], radial migration of embryos themselves and/or

rapid growth facilitated by pebble accretion[32] would have resulted in growth of embryos to several tenths of Earth masses. These bodies would have retained substantial primary atmospheres of H_2 with surface temperatures above 2,000 K, well above the solidus[19]. The threshold mass for accretion of a H_2-rich atmosphere with surface temperatures above the silicate solidus of about 1,500 K is about 0.2 $M_\oplus$. As discussed above, once an embryo has accreted an optically thick H_2 envelope, these temperatures can persist for as long as an optically thick atmosphere is present.

We explored the consequences of chemical exchange between H_2 atmospheres and magma oceans for the chemical evolution of planetary embryos that formed the Earth. The model is composed of 25 phase components, including enstatite ($MgSiO_3$), magnesium oxide (MgO), silicon dioxide (SiO_2), ferrosilite ($FeSiO_3$), iron oxide (FeO), sodium metasilicate (Na_2SiO_3), sodium oxide (Na_2O), H_2, water (H_2O), carbon monoxide (CO) and carbon dioxide (CO_2) species in silicate melts, iron (Fe), silicon (Si), oxygen (O) and H in metal melts, and H_2, CO, CO_2, methane (CH_4), O_2, H_2O, Fe, magnesium (Mg), sodium (Na) and silicon monoxide (SiO) in the atmospheres. This system spans a reaction space of 18 linearly independent reactions that account for speciation in the magma ocean, exchange between the atmosphere and the magma ocean, and exchange between silicate and metal in the magma ocean. For each of the 18 independent reactions, we solved the conditions for thermodynamic equilibrium together with the mass-balance constraints for the atmosphere, silicate melt and metal melt, as well as the pressure at the base of the atmosphere as prescribed by the mean molecular weight of the atmosphere and gravitational acceleration (Methods). Solutions were obtained by a combination of simulated annealing and Markov chain Monte Carlo (MCMC) sampling (Methods), as described previously by ref. [20]. This chemical system is meant to be simple enough to interpret but sufficiently complex to account for the salient features of atmosphere–magma ocean exchange.

Although we assumed ideal mixing for the atmosphere and silicate melt (Methods), precise concentrations of light elements in the metal are a focus of our study, so in this case we used the non-ideal mixing model for the alloying species O, Si and Fe given by ref. [33]. The thermodynamic mixing behaviour of H in Fe metal is not as well characterized. However, ideal mixing as a first approximation is suggested by the small size of H atoms forming interstitial alloys with Fe. Recent results[34] showing that H bonds mainly with Fe in metal with no preference for bonding with O lend support for this approximation. The effects of non-ideal mixing of H in the metal alloy are described in Methods.

We used a fiducial embryo mass of 0.5 $M_\oplus$ for illustration, although our results are not critically dependent on the precise masses of the embryos as long as they exceed about 0.2 $M_\oplus$. The initial composition of the body is composed of an Fe metal fraction of 34.4%, resulting in a final metal alloy mass fraction of 32.5% in our models, consistent with Earth's core fraction. The initial silicate is consistent with estimates for the bulk silicate Earth projected into the model composition space composed of Mg, Si, Fe, Na and O (that is, excluding calcium (Ca) and aluminium (Al)). We assumed the initial concentration of total oxidized Fe, where all Fe in the silicate is cast as FeO for reporting purposes, to be 0.07 wt% to simulate the reduced nature of the inner Solar System as evidenced by E chondrites and Mercury ($\Delta IW \approx -5$ compared with $\Delta IW \approx -2$ for Earth where IW refers to the iron-wüstite oxygen buffer; see below).

We performed calculations over a range of metal–silicate equilibration temperatures and corresponding potential temperatures at the top of the magma ocean (Fig. 1). A metal–silicate equilibration temperature of 3,000 K was adopted as our fiducial model as this is the temperature indicated by element partitioning between Earth's silicate and metal at pressures of about 40 GPa for single-stage and multi-stage equilibration models involving progressively increasing oxygen fugacities[35]. This allows for either inheritance of metal–silicate elemental partitioning from Earth's progenitor planetary embryos or subsequent re-equilibration following, for example, the giant impact that formed the Moon, as suggested by the hafnium–tungsten isotopic system[35]. On the basis of a Vinet equation of state (EOS) for the molten metal core[20,36–38] and a third-order Birch–Murnaghan EOS for the silicate[36], the pressure at the core–mantle boundary of a fully differentiated 0.5 $M_\oplus$ body with Earth-like fractions of metal is about 60 GPa (Methods), suggesting the possibility of equilibration at depths shallower than the core–mantle boundary in these models (as in the case of Earth itself). Embryo masses of 0.3 $M_\oplus$ result in a core–mantle boundary pressure of 40 GPa. For our fiducial case, the potential temperature of the magma ocean of 2,350 K is used for the surface of the magma ocean, reflecting the thermal insulating effect of the dense, optically thick H_2 atmospheres. The initial pressure of the primary atmosphere in our favoured solution is 0.13 GPa (1,338 bar), corresponding to a total H mass fraction of about 0.2%, which is within the range of predicted H mass fractions from atmospheric accretion models[19]. The potential temperature varies by approximately 100 K depending on whether the 3,000 K equilibration occurs above the final core–mantle boundary at 40 GPa or at the final core–mantle boundary at 60 GPa. Our results are not sensitive to this uncertainty in pressure.

The results show that the overall effect of reaction between magma oceans and H_2-rich primary atmospheres is transfer of large masses of H_2 to the metal phase, oxidation of the atmosphere and production of significant quantities of H_2O (Fig. 1). The production of H_2O by reactions between H_2 atmospheres and the underlying planet has been pointed out previously[39,40]. Here we find that the conditions for production of H_2O by the coupled equilibria are accompanied by incorporation of H into the metal phase. Light elements in the metal cores and total H_2O are positively correlated, illustrating that H_2O is a by-product of the redox reactions that drive H into the metal. H_2O is also a product of oxidation of the atmosphere by evaporation of oxides comprising the silicate melt[20]. H_2O produced in the interiors of the embryos and in the atmosphere partitions according to the solubility of H_2O in the magma ocean. Partitioning between melt and atmosphere is sensitive to the activity–composition relationship for H_2O in the melt (for example, dissolution of H_2O as OH shifts more water to the melt in Fig. 1b).

Both Si and O are also incorporated into metal as the embryos equilibrate in these calculations, contributing to the density deficits in the metal relative to pure Fe. Earth is known to have a density deficit relative to pure Fe (+nickel (Ni)) of about 10%[41]. The Birch–Murnaghan EOS for Fe–H alloy determined by ref. [42] shows that the density deficit caused by H at 3,000 K and 40 GPa increases by up to 25% when compressed to 136 GPa at temperatures >4,000 K, the conditions for Earth's outermost core. Therefore, a deficit in metal density of 8% relative to pure Fe in the embryos as a result of reactions with H_2-rich primary atmospheres could produce a 10% deficit in Earth's core upon compression. An 8% density deficit is obtained in our fiducial model for a total H concentration of 0.2% by mass (Fig. 1a). In this case, the calculated metal cores are composed of 94.9% by mass Fe, 3.8% Si, 0.8% O and 0.5% H. Because a density deficit relative to pure Fe of 8.7% results for each weight per cent of H in Fe alloys, whereas the values for O and Si are 1.2% and 0.8%, respectively[43], three-quarters of the density deficit in the cores is attributable to H. For comparison, a 10% density deficit in embryo metal is obtained from a body composed of 0.3% by mass H (Fig. 1a). At this total H content, the calculated metal cores are composed of 94.6% by mass Fe, 3.8% Si, 0.9% O and 0.7% H.

The H mass fraction of about 0.2% that corresponds to an embryo metal density deficit of 8% also produces a mass fraction of H_2O corresponding to approximately one terrestrial ocean (Fig. 1b). For a total H mass fraction of 0.3%, corresponding to a 10% density deficit in the embryo cores, the fractional amount of H_2O produced is about 2 to 3 ocean equivalents. These results are similar to that of an earlier study on production of H_2O by oxidation of atmospheric H_2 (ref. [39]). Even if the rocks in the inner Solar System were entirely dry, reactions between H_2 atmospheres and magma oceans would generate copious amounts of H_2O. Other sources of H_2O are possible, but not required.

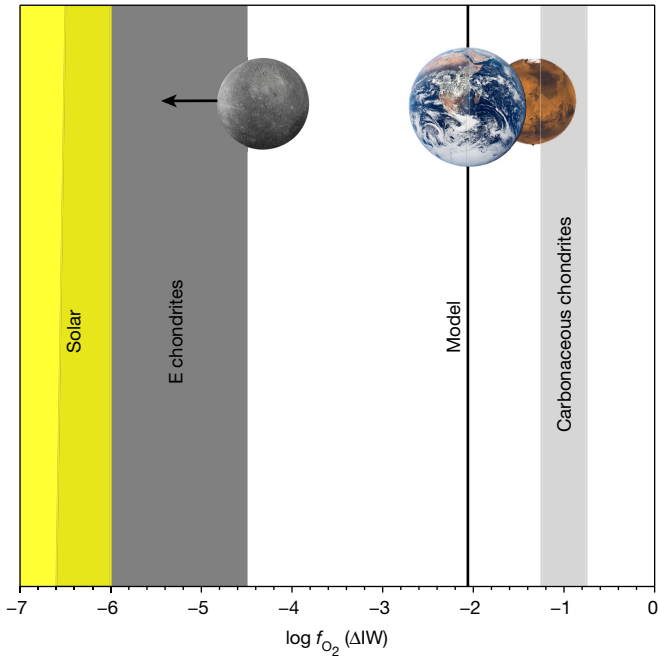

Fig. 2 | Comparison of oxygen fugacities in the Solar System. The model for equilibration between magma oceans and H_2-rich atmospheres (vertical black line) results in an increase in oxygen fugacity from values similar to Mercury and E chondrites, representing the inner Solar System, to the value for Earth. This figure compares the model oxygen fugacity for embryos matching Earth with values from the Solar System, including those for a solar gas, E chondrites, carbonaceous chondrites, Mercury, Earth and Mars. All values are intrinsic oxygen fugacities based on bulk silicate FeO concentrations[44] and are reported as log f_{O_2} relative to the iron-wüstite buffer. The value for Mercury is actually a range from about −4 to −6, depending on the study. The images of Mercury, Earth and Mars are from NASA.

Earth's intrinsic oxidation state as recorded by the amount of FeO in the bulk silicate Earth derived from our calculations is consistent with the observed value. This is a measure of self-consistency between the oxidation state of the planet and the composition of the metal core afforded by this model. The oxidation state of silicates in planetary bodies is usually reported in terms of oxygen fugacity, or the non-ideal partial pressure of oxygen that would be defined by equilibrium with the silicate if O_2 were exchanged between a vapour phase and the melt. By convention, oxygen fugacities are reported relative to the reaction between pure Fe and pure FeO (wüstite) according to the reaction $Fe + 1/2O_2 = FeO$ as $\Delta IW = 2\log(x_{FeO}/x_{Fe})$, where x_{FeO} is the mole fraction of FeO (as total Fe) in the silicate and x_{Fe} is the mole fraction of Fe in metal, assuming ideal mixing (again, by convention). On this scale, E chondrites and aubrites have ΔIW values of about −4.5 to −6.5, similar to an H_2-rich solar gas, and Earth has a value of about −2.2 (ref. [44]; Fig. 2). We used an E chondrite value of −5.8 as our initial condition. Equilibration of the system yields an Earth-like ΔIW of about −2.1 as a result of oxidation of Fe displaced from the core by Si, a process that can be written as $Si^{4+} + 2Fe^0 = Si^0 + 2Fe^{2+}$, which has been suggested previously as a mechanism for oxidizing the mantle[3,45]. Although this process can occur in the absence of H, our calculations show that the Earth's intrinsic oxidation state is consistent with its core density that is in turn attributable to equilibration with an H_2 atmosphere. This need not have been the case.

The two adjustable parameters in our calculations, core–mantle temperature of equilibration and the initial mass fraction of H_2, are degenerate with respect to the density of the core. However, to fit the core density with higher temperatures and substantially less H, the density deficit must come from more and more Si and O in the core (arrow in Fig. 1a). More Si (>6 wt%; Extended Data Fig. 2) in the core results in a higher intrinsic oxygen fugacity by several tenths of log units (arrow in Fig. 1c), reaching values greater than estimates for the Earth. In addition, little to no H_2O is formed in the absence of a significant primary H_2 atmosphere (arrows in Fig. 1b), requiring in this case that Earth's H_2O must be entirely exogenous.

Our prediction that the primary light element in Earth's core that is responsible for the density deficit relative to pure Fe and Ni is H has implications for the seismic velocities (V_P) in the outer core. The outer core has a higher V_P relative to pure Fe by several per cent[46]. Both H and Si increase V_P in molten Fe alloys, with the small concentrations of O in our models having negligible effects. The largest effect is expected for H (refs. [47,48]). A previous study[48] showed that for Fe–H alloys similar in composition to those in our models, V_p increases by about 1.8% relative to pure Fe–Ni alloys, and yields values for V_P consistent with the value for the outermost core[49]. The outer-core densities and seismic velocities implied by our model core composition are within about 2% of measured values based on the published EOSs[33,42], which we consider a reasonable fit given differences between models based on different EOSs.

Figure 3 summarizes our proposed model for the evolution of Earth's progenitor embryos with masses on the order of a few tenths of $M_\oplus$. Our fiducial calculation should be regarded as a surrogate for the average of what may be several embryos that eventually combined to form Earth. Equilibration between metal and silicate in planetary embryos provides a natural explanation for the relatively low pressures of about 40 GPa attending element partitioning for Earth compared with Earth's core–mantle boundary pressure of 136 GPa as this lower pressure corresponds to those near the core–mantle boundaries of embryos. The precise masses of Earth's progenitor embryos are not crucial to our conclusions. For example, our modelling results are virtually identical using the smaller embryo mass of 0.3 $M_\oplus$ where 3,000 K and 40 GPa represent the core–mantle boundary. In this case, the potential temperature is 2,535 K, but nonetheless the core composition, H_2O fractions, oxygen fugacity and other model results are unchanged (Supplementary Information).

If this is the explanation for the low pressures of equilibration, core–mantle partitioning was inherited from the embryos from which Earth was built, and many of these chemical signatures survived subsequent collisions among embryos, including the Moon-forming giant impact. The alternative is that melting during giant impacts reset core–mantle equilibrium at similar conditions[35]. Collisions between embryos after the protoplanetary gas disk has dissipated would efficiently remove any residual H_2-dominated atmospheres. However, the H_2O-rich atmospheres left behind by equilibrium between the H_2 primary atmospheres and magma oceans will be largely retained[50]. As a result, most of the water produced in the embryo stage will remain once the disk dissipates[51]. To test the effects of colliding two embryos with residual H_2O atmospheres to produce Earth, we applied our model to an initial condition of a 1-$M_\oplus$ body with mantle, core and H_2O-rich atmosphere compositions corresponding to our final embryo equilibrium state. The results verify that the chemical signature of H_2 on embryos survives subsequent impact-generated re-equilibration at similar temperatures.

In the context of our model for Earth formation involving a primary atmosphere of H_2, both Mars and Mercury are planetary embryos that never reached sufficient mass to allow primary atmospheres of H_2 at magma ocean surface temperatures. The identities of the light elements in the core of Mars are not known with certainty, but are generally believed to be dominated by sulfur (S)[52]. The effect of S on the density deficit of metal alloys is similar to that of Si, and tens of per cent by mass of S are required to account for the density of the core. Also in the context of this model, the relatively high intrinsic oxidation state of Mars (high FeO in silicate, but see also ref. [52]) may be attributable to a large fraction of its mass being derived from beyond 2 AU where the more oxidized and H_2O-rich carbonaceous chondrites could serve as

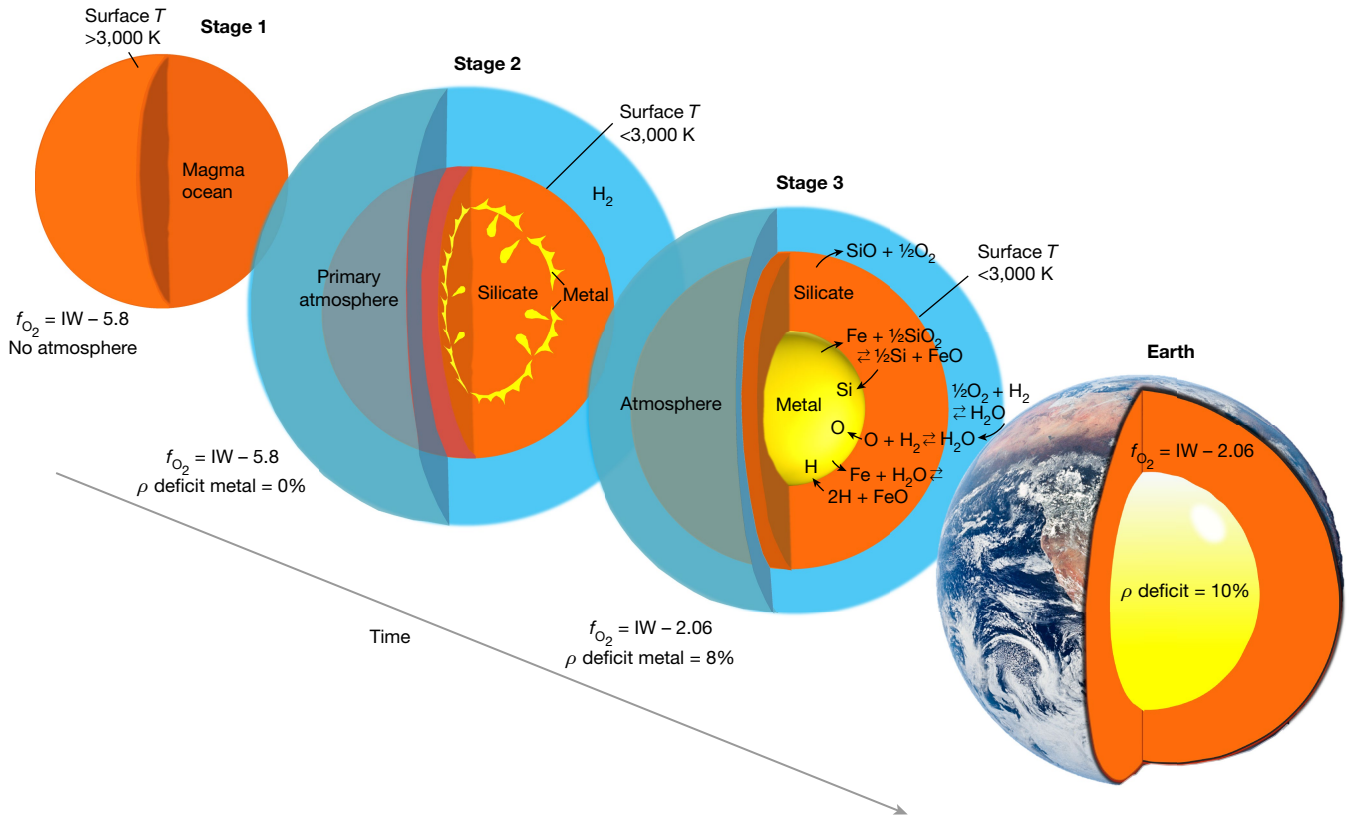

Fig. 3 | Proposed model for the evolution of Earth's progenitor embryos. The sequence of events leading to formation of H_2O, light elements in metal and increases in oxygen fugacity for Earth's progenitor embryos in this work. Stage 1 is the embryo where surface temperatures are too high to retain primary atmospheres of H_2. Stage 2 is the initial condition for our calculations in which the molten embryos accrete and retain primary atmospheres of H_2. Metal–silicate differentiation may have already begun at this stage. Stage 3 is the result of chemical equilibration of the silicate and metal melts with the evolved atmospheres. Annotations show the changes in oxygen fugacity and metal density deficits. Reactions shown are simplifications of the full set, for illustration purposes. Two or more such embryos combine to form the final Earth. The image of Earth is from NASA.

sources[53]. In the case of Mercury, if one assumes that the large metal fraction of Mercury is due to stripping of its mantle[54], and that the original mass fraction of its metal core was similar to that of Earth (0.32), then the mass of the original body was between 0.09 $M_\oplus$ and 0.13 $M_\oplus$ for a range of estimated present-day core fractions of 55% to 75% by mass[55,56]. Like Mars, this is not sufficiently massive to retain a H_2 atmosphere at super-solidus temperatures. The light element in the Mercurian core is thought to be mainly Si, with lesser concentrations of S and no clear evidence for H. Therefore, the chemical distinction between Earth and these stranded embryos may in part be that Earth was built from embryos that reached sufficient mass to retain H_2-rich atmospheres at super-solidus surface temperatures.

Our model does not include S and we do not exclude the possibility that the details of the model might change if S were included. Similarly, we do not include carbon or nitrogen as potential interstitial alloying elements in the core. Omission of Ni is not expected to have a significant effect. Although details of our conclusions may change, the essential point that reactions with H_2-rich atmospheres are effective in producing both H_2O and density deficits in metal cores remains robust, as does the result that the silicate mantles of progenitor embryos resembling E chondrites and Mercury in having low total FeO, should have 'self-oxidized' to Earth-like oxidation states given sufficient time to approach equilibrium[45]. We provide a discussion of the isotopic consequences of our results in Methods.

This study makes use of what we have learned from rocky exoplanets about the potential importance of primary H_2-rich atmospheres to terrestrial planet formation in general. The result is a unified, self-consistent explanation for a number of important features of Earth related by a single overarching process of oxidation and reduction (redox) chemistry triggered by reactions between H_2 and magma oceans. Although it is possible that Earth formed in a very different way from the majority of rocky exoplanets, our work shows that this need not be the case and that we can place the formation of Earth into the context of rocky planet formation across the Galaxy.

Online content

Any methods, additional references, Nature Portfolio reporting summaries, source data, extended data, supplementary information, acknowledgements, peer review information; details of author contributions and competing interests; and statements of data and code availability are available at https://doi.org/10.1038/s41586-023-05823-0.

1. Bean, J. L., Raymond, S. N. & Owen, J. E. The nature and origins of sub-Neptune size planets. *J. Geophys. Res. Planets* **126**, e06639 (2021).
2. Wetherill, G. W. Accumulation of the terrestrial planets. in *IAU Colloquium 52: Protostars and Planets* (eds Gehrels, T. & Matthews, M. S.) 565 (Univ. Arizona Press, 1978).
3. Rubie, D. et al. Accretion and differentiation of the terrestrial planets with implications for the compositions of early-formed Solar System bodies and accretion of water. *Icarus* **248**, 89–108 (2015).
4. Albarède, F. Volatile accretion history of the terrestrial planets and dynamic implications. *Nature* **461**, 1227–1233 (2009).
5. Cartier, C. & Wood, B. J. The role of reducing conditions in building Mercury. *Elements* **15**, 39–45 (2019).
6. Dauphas, N. The isotopic nature of the Earth's accreting material through time. *Nature* **541**, 521–524 (2017).
7. Sikdar, J. & Rai, V. K. Si–Mg isotopes in enstatite chondrites and accretion of reduced planetary bodies. *Sci. Rep.* **10**, 1273 (2020).
8. Javoy, M. The integral enstatite chondrite model of the Earth. *Geophys. Res. Lett.* **22**, 2219–2222 (1995).

9. Nittler, L. R. et al. The major-element composition of Mercury's surface from messenger X-ray spectrometry. *Science* **333**, 1847–1850 (2011).
10. Shepard, M. K. et al. A radar survey of M- and X-class asteroids. III. Insights into their composition, hydration state, & structure. *Icarus* **245**, 38–55 (2015).
11. Zellner, B., Leake, M., Morrison, D. & Williams, J. The E asteroids and the origin of the enstatite achondrites. *Geochim. Cosmochim. Acta* **41**, 1759–1767 (1977).
12. Piani, L. et al. Earth's water may have been inherited from material similar to enstatite chondrite meteorites. *Science* **369**, 1110–1113 (2020).
13. Petigura, E. A., Howard, A. W. & Marcy, G. W. Prevalence of Earth-size planets orbiting Sun-like stars. *Proc. Natl Acad. Sci. USA* **110**, 19273–19278 (2013).
14. Weiss, L. M. & Marcy, G. W. The mass–radius relation for 65 exoplanets smaller than 4 Earth radii. *Astrophys. J.* **783**, L6 (2014).
15. Fulton, B. J. et al. The California–Kepler survey. III. A gap in the radius distribution of small planets. *Astrophys. J.* **154**, 109 (2017).
16. Berger, T. A., Huber, D., Gaidos, E., van Saders, J. L. & Weiss, L. M. The Gaia–Kepler Stellar Properties Catalog. II. Planet radius demographics as a function of stellar mass and age. *Astron. J.* **160**, 108 (2020).
17. Owen, J. E. & Wu, Y. Kepler planets: a tale of evaporation. *Astrophys. J.* **775**, 105 (2013).
18. Gupta, A. & Schlichting, H. E. Sculpting the valley in the radius distribution of small exoplanets as a by-product of planet formation: the core-powered mass-loss mechanism. *Mon. Not. R. Astron. Soc.* **487**, 24–33 (2019).
19. Ginzburg, S., Schlichting, H. E. & Sari, R. Super-Earth atmospheres: self-consistent gas accretion and retention. *Astrophys. J.* **825**, 29 (2016).
20. Schlichting, H. E. & Young, E. D. Chemical equilibrium between cores, mantles, and atmospheres of super-Earths and sub-Neptunes, and implications for their compositions, interiors and evolution. *Planet. Sci. J.* **9**, 127 (2022).
21. Solomatov, V. S. *Magma Oceans and Primordial Mantle Differentiation* Vol. 9 (Elsevier, 2009).
22. Young, E. D. et al. Near-equilibrium isotope fractionation during planetesimal evaporation. *Icarus* **323**, 1–15 (2019).
23. Mukhopadhyay, S. Early differentiation and volatile accretion recorded in deep-mantle neon and xenon. *Nature* **486**, 101–104 (2012).
24. Mukhopadhyay, S. & Parai, R. Noble gases: a record of Earth's evolution and mantle dynamics. *Annu. Rev. Earth Planet. Sci.* **47**, 389–419 (2019).
25. Williams, C. D. & Mukhopadhyay, S. Capture of nebular gases during Earth's accretion is preserved in deep-mantle neon. *Nature* **565**, 78–81 (2019).
26. Lammer, H. et al. Constraining the early evolution of Venus and Earth through atmospheric Ar, Ne isotope and bulk K/U ratios. *Icarus* **339**, 113551 (2020).
27. Sharp, Z. & Olson, P. Multi-element constraints on the sources of volatiles to earth. *Geochim. Cosmochim. Acta* **333**, 124–135 (2022).
28. Kurokawa, H. et al. Mars' atmospheric neon suggests volatile-rich primitive mantle. *Icarus* **370**, 114685 (2021).
29. Peron, S. & Mukhopadhyay, S. Krypton in the Chassigny meteorite shows Mars accreted chondritic volatiles before nebular gases. *Science* **377**, 320–324 (2022).
30. Dauphas, N. & Pourmand, A. Hf–W–Th evidence for rapid growth of Mars and its status as a planetary embryo. *Nature* **473**, 489–492 (2011).
31. Schlichting, H. E. Formation of close in super-Earths and mini-Neptunes: required disk masses and their implications. *Astrophys. J.* **795**, L15 (2014).
32. Johansen, A. et al. A pebble accretion model for the formation of the terrestrial planets in the Solar System. *Sci. Adv.* **7**, eabc0444 (2021).
33. Badro, J., Brodholt, J. P., Piet, H., Siebert, J. & Ryerson, F. Core formation and core composition from coupled geochemical and geophysical constraints. *Proc. Natl Acad. Sci. USA* **112**, 12310–12314 (2015).
34. Li, Y., Vočadlo, L., Sun, T. & Brodholt, J. P. The Earth's core as a reservoir of water. *Nat. Geosci.* **13**, 453–458 (2020).
35. Wood, B. Accretion and core formation: constraints from metal-silicate partitioning. *Phil. Trans. R. Soc. Lond. A* **366**, 4339–4355 (2008).
36. Seager, S., Kuchner, M., Hier-Majumder, C. A. & Militzer, B. Mass–radius relationships for solid exoplanets. *Astrophys. J.* **669**, 1279–1297 (2007).
37. Anderson, O. L., Dubrovinsky, L., Saxena, S. K. & LeBihan, T. Experimental vibrational Grüneisen ratio values for ∈-iron up to 330 GPa at 300 K. *Geophys. Res. Lett.* **28**, 399–402 (2001).
38. Kuwayama, Y. et al. Equation of state of liquid iron under extreme conditions. *Phys. Rev. Lett.* **124**, 165701 (2020).
39. Ikoma, M. & Genda, H. Constraints on the mass of a habitable planet with water of nebular origin. *Astrophys. J.* **648**, 696–706 (2006).
40. Kite, E. & Schaefer, L. Water on hot rocky exoplanets. *Astrophys. J. Lett.* **909**, L22 (2021).
41. Birch, F. Density and composition of mantle and core. *J. Geophys. Res.* **69**, 4377–4388 (1964).
42. Umemoto, K. & Hirose, K. Chemical compositions of the outer core examined by first principles calculations. *Earth Planet. Sci. Lett.* **531**, 116009 (2020).
43. Li, J., Chen, B., Mookherjee, M. & Morard, G. *Carbon versus Other Light Elements in Earth's Core* 40–65 (Cambridge Univ. Press, 2019).
44. Doyle, A. E., Young, E. D., Klein, B., Zuckerman, B. & Schlichting, H. E. Oxygen fugacities of extrasolar rocks: evidence for an Earth-like geochemistry of exoplanets. *Science* **366**, 356–359 (2019).
45. Javoy, M. et al. The chemical composition of the Earth: enstatite chondrite models. *Earth Planet. Sci. Lett.* **293**, 259–268 (2010).
46. Dziewonski, A. M. & Anderson, D. L. Preliminary reference Earth model. *Phys. Earth Planet. Inter.* **25**, 297–356 (1981).
47. Sanloup, C., Fiquet, G., Gregoryanz, E., Morard, G. & Mezouar, M. Effect of Si on liquid Fe compressibility: implications for sound velocity in core materials. *Geophys. Res. Lett.* **31**, L07604 (2004).
48. Umemoto, K. & Hirose, K. Liquid iron–hydrogen alloys at outer core conditions by first-principles calculations. *Geophys. Res. Lett.* **42**, 7513–7520 (2015).
49. Kennett, B. L. N., Engdahl, E. R. & Buland, R. Constraints on seismic velocities in the Earth from traveltimes. *Geophys. J. Int.* **122**, 108–124 (1995).
50. Biersteker, J. B. & Schlichting, H. E. Losing oceans: the effects of composition on the thermal component of impact-driven atmospheric loss. *Mon. Not. R. Astron. Soc.* **501**, 587–595 (2021).
51. Biersteker, J. B. & Schlichting, H. E. Atmospheric mass-loss due to giant impacts: the importance of the thermal component for hydrogen–helium envelopes. *Mon. Not. R. Astron. Soc.* **485**, 4454–4463 (2019).
52. Stähler, S. C. et al. Seismic detection of the Martian core. *Science* **373**, 443–448 (2021).
53. Brasser, R. The formation of Mars: building blocks and accretion time scale. *Space Sci. Rev.* **174**, 11–25 (2013).
54. Benz, W., Anic, A., Horner, J. & Whitby, J. A. The origin of Mercury. *Space Sci. Rev.* **132**, 189–202 (2007).
55. Riner, M. A., Bina, C. R., Robinson, M. S. & Desch, S. J. Internal structure of Mercury: implications of a molten core. *J. Geophys. Res. Planets* **113**, E08013 (2008).
56. Margot, J.-L., Hauck, S. A., Mazarico, E., Padovan, S. & Peale, S. J. *Mercury's Internal Structure* 85–113 (Cambridge Univ. Press, 2018).

Methods

Chemical thermodynamics

The linearly independent reactions spanning our reaction space, and strategies for solving the coupled thermodynamic and mass-balance equations, have been described previously in ref. [20] and are described here briefly. The reactions comprising our model include speciation reactions in the magma ocean:

$$Na_2SiO_3 \rightleftharpoons Na_2O + SiO_2, \quad (1)$$

$$1/2SiO_2 + Fe_{metal} \rightleftharpoons FeO + 1/2Si_{metal}, \quad (2)$$

$$MgSiO_3 \rightleftharpoons MgO + SiO_2, \quad (3)$$

$$O_{metal} + 1/2Si_{metal} \rightleftharpoons 1/2SiO_2, \quad (4)$$

$$2H_{metal} \rightleftharpoons H_{2,silicate}, \quad (5)$$

$$FeSiO_3 \rightleftharpoons FeO + SiO_2, \quad (6)$$

$$2H_2O_{silicate} + Si_{metal} \rightleftharpoons SiO_2 + 2H_{2,silicate}, \quad (7)$$

reactions that take place in the atmosphere:

$$CO_{gas} + 1/2O_{2,gas} \rightleftharpoons CO_{2,gas}, \quad (8)$$

$$CH_{4,gas} + 1/2O_{2,gas} \rightleftharpoons 2H_2 + CO, \quad (9)$$

$$H_{2,gas} + 1/2O_{2,gas} \rightleftharpoons H_2O_{gas}, \quad (10)$$

and reactions that describe exchange between the atmosphere and the magma ocean:

$$FeO \rightleftharpoons Fe_{gas} + 1/2O_{2,gas}, \quad (11)$$

$$MgO \rightleftharpoons Mg_{gas} + 1/2O_{2,gas}, \quad (12)$$

$$SiO_2 \rightleftharpoons SiO_{gas} + 1/2O_{2,gas}, \quad (13)$$

$$Na_2O \rightleftharpoons 2Na_{gas} + 1/2O_{2,gas}, \quad (14)$$

$$H_{2,gas} \rightleftharpoons H_{2,silicate}, \quad (15)$$

$$H_2O_{gas} \rightleftharpoons H_2O_{,silicate} \quad (16)$$

$$CO_{gas} \rightleftharpoons CO_{silicate}, \quad (17)$$

$$CO_{2,gas} \rightleftharpoons CO_{2,silicate}. \quad (18)$$

For each of the 18 reactions (rxns) among the 25 phase components described above, there is an equation for the condition for equilibrium. These equations are of the form

$$\sum_i \nu_i \ln x_i + \left[\frac{\Delta \hat{G}^{o}_{rxn}}{RT} + \sum_g \nu_g \ln(P/P^{o})\right] = 0. \quad (19)$$

Here we have used $\mu_i = \Delta\hat{G}_i^{o} + RT\ln(x_i)$ for the chemical potential of species i corrected for composition, where $\Delta\hat{G}_i^{o}$ is the molar Gibbs free energy of formation of i at a standard state of the pure species at temperature and 1-bar pressure, x_i is the mole fraction for species i in the host phase, ν_i is the stoichiometric coefficient for i in the reaction, T is the temperature and R is the gas constant. The sum over index g refers to gas species in the reaction and index i refers to all species, including the gases. We separated the compositional and pressure effects for the gas species, replacing partial pressure (ideal fugacity), for species g, by the product x_gP, where P is the total gas pressure and P^{o} is the pressure at standard state (chosen as 1 bar here).

Following ref. [33], we replaced mole fractions for Si and O in equation (19) with activities a_i where $a_i = \gamma_i x_i$ to account for non-ideal competition between O and Si in the metal phase. The activity coefficient for Si, γ_{Si}, is given by

$$\begin{aligned}\ln\gamma_{Si} = &-6.65\frac{1{,}873}{T} - 12.41\frac{1{,}873}{T}\ln(1-x_{Si}) \\ &+ 5\frac{1{,}873}{T}x_O\left(1 + \frac{\ln(1-x_O)}{x_O} - \frac{1}{(1-x_{Si})}\right) \\ &- 5\frac{1{,}873}{T}x_O^2 x_{Si}\left(\frac{1}{1-x_{Si}} + \frac{1}{1-x_O} + \frac{x_{Si}}{2(1-x_{Si})^2} - 1\right),\end{aligned} \quad (20)$$

and the activity coefficient for O, γ_O, is obtained using

$$\begin{aligned}\ln\gamma_{O} = &\ 4.29 - \frac{16{,}500}{T} + \frac{16{,}500}{T}\ln(1-x_O) \\ &+ 5\frac{1{,}873}{T}x_{Si}\left(1 + \frac{\ln(1-x_{Si})}{x_{Si}} - \frac{1}{(1-x_O)}\right) \\ &- 5\frac{1{,}873}{T}x_{Si}^2 x_O\left(\frac{1}{1-x_O} + \frac{1}{1-x_{Si}} + \frac{x_O}{2(1-x_O)^2} - 1\right).\end{aligned} \quad (21)$$

The activity coefficient for Fe in metal using this approach is near unity (for example, 0.8 (ref. [57])). We assume $\gamma_{Fe} = 1$ given the uncertainties in mixing parameters involving H in metal. The mixing behaviour of H in liquid Fe metal at high pressures is not as well characterized. We therefore adopt ideal mixing for H in Fe metal. Recent results in ref. [34] suggest that H pairs mainly with Fe in metal with no preference for bonding with O, consistent with composition-independent, ideal mixing.

Ideal mixing is assumed for silicate melt species. Ideal mixing as applied here has been validated using the MAGMA code[58,59] where speciation of simple oxides such as FeO and MgO to silicate species such as $FeSiO_3$ and $MgSiO_3$ accounts for first-order activity and composition effects[60]. Further discussion of the effects of non-ideal mixing on our results is presented below.

To these equations, we add an additional seven equations that account for the summing constraints for each of the seven elements making up the body:

$$n_s - \sum_k \sum_i \eta_{s,i,k} x_{i,k} N_k = 0, \quad (22)$$

where n_s is the moles of element s in the planet, $\eta_{s,i,k}$ is the number of moles of element s in component i of phase k, $x_{i,k}$ is the mole fraction of component i in phase k, and N_k is the moles of phase k (metal, silicate or atmosphere). The moles of the phases are treated as variables along with the mole fractions for the species, resulting in 28 variables in the system of equations. The mole fractions for each phase must sum to unity, so our new equations include

$$\begin{aligned}&1 - x_{MgO} - x_{SiO_2} - x_{MgSiO_3} - x_{FeO} - x_{FeSiO_3} - x_{Na_2O} \\ &- x_{Na_2SiO_3} - x_{H_2}^{silicate} - x_{H_2O}^{silicate} - x_{CO}^{silicate} - x_{CO_2}^{silicate} = 0\end{aligned} \quad (23)$$

for the silicate phase,

$$1 - x_{\mathrm{Fe}}^{\mathrm{metal}} - x_{\mathrm{Si}}^{\mathrm{metal}} - x_{\mathrm{O}}^{\mathrm{metal}} - x_{\mathrm{H}}^{\mathrm{metal}} = 0 \quad (24)$$

for the metal phase, and

$$1 - x_{\mathrm{CO}}^{\mathrm{gas}} - x_{\mathrm{CO_2}}^{\mathrm{gas}} - x_{\mathrm{O_2}}^{\mathrm{gas}} - x_{\mathrm{CH_4}}^{\mathrm{gas}} - x_{\mathrm{H_2}}^{\mathrm{gas}} - x_{\mathrm{H_2O}}^{\mathrm{gas}} - x_{\mathrm{Fe}}^{\mathrm{gas}} - x_{\mathrm{Mg}}^{\mathrm{gas}} - x_{\mathrm{SiO}}^{\mathrm{gas}} - x_{\mathrm{Na}}^{\mathrm{gas}} = 0 \quad (25)$$

for the atmosphere.

The atmospheric pressure at the surface of the magma ocean, P_{surface} is an additional variable that depends on the mean molecular weight of the atmosphere, and thus must be included in the solutions. This is accomplished by adding the equation

$$\left(\frac{P_{\mathrm{surface}}}{1\ \mathrm{bar}}\right) = 1.2 \times 10^6 \frac{M_{\mathrm{atm}}}{M_{\mathrm{p}}} \left(\frac{M_{\mathrm{p}}}{M_{\oplus}}\right)^{2/3} \quad (26)$$

to the system of equations to be solved, where the mass of the atmosphere, M_{atm}, is obtained from the molecular weight and the moles of the atmosphere, N_{atm}.

The 29 nonlinear equations in 29 variables were solved using simulated annealing followed by MCMC sampling. We used the Python implementation of simulated annealing[61] and the MIT Python implementation of ensemble MCMC[62,63]. The combination of simulated annealing followed by MCMC sampling avoids becoming stranded in local minima. We used the thermodynamic data, including the treatment of H_2 solubility, described in detail in ref. [20], with the exception that we replaced the free energy of reaction for reaction (2) with that given by ref. [57]. The use of free energies for the reactions permits application of self-consistent free energies of formation for the various species in our reaction network, and supplants distribution coefficients for partitioning of elements between phases that are not necessarily internally consistent.

Embryo primary atmospheres

Extended Data Fig. 1 shows the relationship between the mass of planetary embryos, their surface temperatures, and the potential coexistence of a surface magma ocean and H_2-rich primary atmospheres following ref. [19]. The boundary between solid and liquid silicate at the condensed surface is taken to be 1,500 K in the figure. Mars is shown to be sufficiently massive to have had a primary atmosphere, but not massive enough to have this atmosphere in coexistence with a surface magma ocean. The crossing of the two blue lines in the figure defines the minimum mass for an embryo to have simultaneously a primary H_2-rich atmosphere and a surface magma ocean.

Silicon in metal

Extended Data Fig. 2 shows our results for the weight per cent of Si in metal as a function of core–mantle equilibration temperature and initial mass fraction of the H_2-rich primary atmosphere. This figure is comparable to the panels shown in Fig. 1.

Sensitivity tests

We examined the effects of the assumption of ideal mixing between H_2O and silicate and between H_2 and silicate on our results. We also evaluated the effects of non-ideal mixing of H in the Fe metal alloy phase. Our fiducial model recalculated to include all of these potential non-ideal mixing behaviours is shown in Supplementary Table 4 and can be compared directly with the results given in Supplementary Table 1. Details of the non-ideal mixing models are provided in this section.

A previous study[64] reported complete miscibility between H_2O and $MgSiO_3$ at temperatures down to 4,500 K at 40 GPa, and at higher temperatures at higher pressures. Extrapolation to the approximately 100-bar surface pressures in our models suggests a consolute temperature, T_c, of about 4,000 K by analogy with supercritical silicate liquid and vapour[65]. Assuming a symmetrical (regular) mixing model based on this observation, an activity coefficient for H_2O in melt can be obtained from $\ln\gamma_{\mathrm{H_2O}}^{\mathrm{silicate}} = (1 - x_{\mathrm{H_2O}}^{\mathrm{silicate}})^2 W/(RT)$, where the interaction parameter W is given by $W = 2RT_c$ and T_c is the temperature at the crest of the silicate–H_2 solvus. The interaction parameter W for $T_c = 4{,}000$ K is 66,512 J mol^{-1}.

The activity–composition relationship for H_2 in silicate melt is not well characterized. However, we can speculate that non-ideal mixing could be evidenced by complete miscibility between H_2 vapour and silicate melt at sufficiently high temperatures. This speculation is supported by as-yet-unpublished ab initio calculations at University of California, Los Angeles. On the basis of these preliminary calculations, we consider a value for the consolute temperature of 4,500 K for pressures of interest, leading to $W = 74{,}829$ J mol^{-1}.

For H in the liquid Fe alloy we used ϵ interaction parameters. The ϵ notation for interaction parameters is commonly used for alloys, representing a Taylor series expansion for the log of the activity coefficient of interest. In the case of a dilute solute i interaction with species j we can relate ϵ_i^j to binary interaction parameters W using $\epsilon_i^j = -2W/(RT)$. A previous study[66] found values for $\epsilon_{\mathrm{H}}^{\mathrm{Si}}$ in liquid Fe of 3.5 (a ternary interaction parameter) and ref. [67] reports that $\epsilon_{\mathrm{H}}^{\mathrm{O}}$ is similar to $\epsilon_{\mathrm{H}}^{\mathrm{Si}}$. We therefore applied a pseudo-ternary mixing model for H in molten Fe alloy, following ref. [68], such that

$$\begin{aligned}\ln\gamma_{\mathrm{H}} = & -\epsilon_{\mathrm{H}}^{\mathrm{Si}} x'_{\mathrm{Si}} \left(1 + \frac{\ln(1 - x'_{\mathrm{Si}})}{x'_{\mathrm{Si}}} - \frac{1}{1 - x_{\mathrm{H}}}\right) \\ & + \epsilon_{\mathrm{H}}^{\mathrm{Si}} x'^2_{\mathrm{Si}} x_{\mathrm{H}} \left(\frac{1}{(1 - x_{\mathrm{H}})} + \frac{1}{(1 - x'_{\mathrm{Si}})} + \frac{x_{\mathrm{H}}}{2(1 - x_{\mathrm{H}})^2} + 1\right),\end{aligned} \quad (27)$$

where x_{H} is the mole fraction of H in the metal alloy and x'_{Si} is the sum of the mole fractions of Si and O in the metal.

The overall effect of the three non-ideal mixing solution models described here for H_2 and H_2O in silicate and H in Fe metal alloy is a change in the H_2O/H_2 ratio in the silicate melt and a doubling of the mass fraction of the atmosphere with no significant change in the H_2O concentration in the atmosphere (Supplementary Table 4). The density deficit in the metal core changes from 8.0% to 8.2%, a change that would be easily accommodated in our models by slight adjustments to the initial mass fraction of the primary atmosphere. The oxygen fugacity of the mantle is essentially unchanged. We find, therefore, that the effect of inclusion of non-ideal mixing of H_2O and H_2 in silicate melt, and non-ideal mixing of H in Fe alloy, is to increase the efficacy of water production with little change to the other salient features of our results. The reason for the robust nature of our solution is that the concentrations of H_2O and H_2 in the silicate are able to compensate for the changes in thermodynamic activities by virtue of the lever-rule effect; most H exists in the metal phase with the remainder partitioned between the atmosphere, as H_2O, and the silicate melt. The changes in silicate H_2O and H_2 concentrations are due primarily to the activity coefficients for these species, with non-ideal mixing of H in the metal having negligible impact on the results.

As an additional sensitivity test, we considered the effects of altering the precise values for H partitioning between silicate and metal. We do this because although the free energies of formation of H_2 in silicate and H in metal were derived in a self-consistent manner, as described below, these values are associated with unknown uncertainties. For this purpose, we reran our calculations with the logarithm of the equilibrium constant for reaction (5), $\ln K_{\mathrm{eq,R5}} = -\Delta\hat{G}^{\mathrm{o}}_{\mathrm{rxn,R5}}/(RT)$, multiplied by factors of 1.5 and 0.5, respectively.

The standard-state free energy of reaction (5)[20] used here is obtained from $\Delta\hat{G}^{\mathrm{o}}_{\mathrm{rxn,R5}} = \Delta\hat{G}^{\mathrm{o,silicate}}_{\mathrm{H_2}} - 2\Delta\hat{G}^{\mathrm{o,metal}}_{\mathrm{H}}$, where $\Delta\hat{G}^{\mathrm{o,silicate}}_{\mathrm{H_2}}$ at T and 1 bar was obtained from the free energy of the reaction $H_{2,\mathrm{gas}} = H_{2,\mathrm{melt}}$ after ref. [69], and $\Delta\hat{G}^{\mathrm{o}}_{\mathrm{H_2}}$ for gas from the National Institute of Standards and Technology (NIST). The $\Delta\hat{G}^{\mathrm{o}}_{\mathrm{H}}$ for metal was obtained from the reaction

$Fe + H_2O_{melt} = FeO + 2H$ by regression of $\ln K_{eq}$ versus $1/T$ reported by ref. [70] (Okuchi97), yielding $\Delta\hat{G}^{o}_{rxn,Okuchi97} = 143,589.7 - 69.1T$ (J mol^{-1}), $\Delta\hat{G}^{o}_{H_2O}$ for silicate melt using the solubility data of ref. [71] for the reaction $H_2O_{gas} = H_2O_{melt}$ (ref. [20]), and the standard-state free energies of formation for H_2O gas, liquid FeO and Fe from NIST. From these values, $\Delta\hat{G}^{o,metal}_{H} = 1/2(\Delta\hat{G}^{o}_{rxn,Okuchi97} - \Delta\hat{G}^{o}_{FeO} + \Delta\hat{G}^{o}_{Fe} + \Delta\hat{G}^{o,silicate}_{H_2O})$.

Our results with these changes in the logarithm of the equilibrium constant describing partitioning of H between silicate and metal are negligible, with the largest change being a decrease in the mass of the atmosphere in the case of increasing $\Delta\hat{G}^{o}_{rxn,R5}$ by 1.5. In the latter case, the result in Supplementary Table 4 is modified by lowering the pressure of the atmosphere at the magma ocean surface from about 300 bar to about 200 bar with no change in the H_2O-rich composition of the atmosphere and no change in the density deficit of the metal core. In the case of decreasing $\Delta\hat{G}^{o}_{rxn,R5}$ by a factor of two, the results were virtually unchanged. These results can also be understood as the manifestation of the lever rule in which the large amount of H in the metal phase relative to the total mass of H in the other reservoirs dominates the behaviour. To see this, we can describe the activity of H in metal, a_H, as a product of the equilibrium constants for reactions (5) and (15), arriving at the expression $a_H = \sqrt{K_{eq,R5}K_{eq,R15}f_{H_2}}$ where f_{H_2} is the fugacity of H_2 in the atmosphere. In the case of the embryos, the activity of H in the metal alloy exerts influence over the partial pressure (fugacity) of H_2 in the atmosphere due to the high mass of H_2 relative to that in the atmosphere.

Pressure versus radius for embryos

The pressure versus radius relationships described in the text are presented in Extended Data Fig. 3. The pressure–radius relations are obtained by solving for the mass, $m(r)$, contained within a given radius, r (ref. [36])

$$\frac{dm(r)}{dr} = 4\pi r^2\rho(r) \tag{28}$$

together with the requirement for hydrostatic equilibrium

$$\frac{dP(r)}{dr} = -\frac{Gm(r)\rho(r)}{r^2}, \tag{29}$$

where

$$P(r) = f(\rho(r), T(r)), \tag{30}$$

and f represents the appropriate EOS. $P(r)$, $\rho(r)$ and $T(r)$ are the radially dependent pressure, density and temperature of the body, respectively, and G is the gravitational constant.

We integrate equations (28) and (29) from the embryo's centre, using the inner boundary condition $m(0) = 0$ and $P(0) = P_{centre}$. The outer boundary condition is given by $P(R_p) = 0$. We switch from one EOS to the other while maintaining continuity in pressure across the core–mantle boundary. The embryo mass, M_p and radius, R_p, are uniquely determined by $P(0) = P_{centre}$ and $P(R_p) = 0$ for the Earth-like mass fractions for the metal core used in our models.

Extrapolation of the data of ref. [38] yields an uncompressed density for liquid Fe metal, ρ_0, of 7.2 ± 0.1 g cm^{-3}. We used this uncompressed density for liquid Fe with a Vinet EOS[36,37]. For the silicate we use the enstatite ($MgSiO_3$) third-order Birch–Murnaghan EOS of ref. [72] described by ref. [36] as a proxy for silicate melt.

Adiabatic temperature gradients for the embryo mantles were calculated using

$$\left(\frac{dT}{dr}\right)_S = \frac{\alpha g T}{c_P} \tag{31}$$

where α is the expansivity for $MgSiO_3$, c_P is the isobaric specific heat for the melt and g is the gravitational acceleration. We used $\alpha = 2.69 \times 10^{-5} + 2.13 \times 10^{-8}(T - 300)$ from ref. [73] with a pressure correction factor of 1.04 for the mantle as a whole. Temperature-dependent c_P for liquid $MgSiO_3$ was obtained from the NIST thermodynamic database. Numerical integrations with r yield a general relationship between potential temperature and core–mantle temperature such that $T_\Theta/T_{core-mantle} \approx 0.78$.

Isotope fractionation

We investigated the implications of our model for Fe, Si and H stable isotope ratios, as these ratios are often used to constrain the differentiation history of Earth[74,75] and the origin of Earth's water[76].

We find that the embryo partitioning model explains the offset in $^{57}Fe/^{54}Fe$ (expressed as $\delta^{57}Fe$ in per mil (‰) between chondrites of all varieties and the bulk silicate Earth. Recent estimates suggest that bulk silicate Earth has a $\delta^{57}Fe = 0.05 \pm 0.01$ value relative to chondrites[77]. This offset between Earth and its presumed starting materials is reproduced by our model shift in bulk silicate $\delta^{57}Fe$ of 0.057‰ relative to the bulk starting material (Extended Data Fig. 4).

We used the prescription for $^{57}Fe/^{54}Fe$ fractionation as a function of temperature and pressure determined experimentally by ref. [78]. The reduced partition function ratio, β, for the silicate is given by

$$10^3\ln(\beta_{Fe-silicate}) = \frac{4{,}281.4(4.65P(\text{GPa}) + 150.4)}{T^2}. \tag{32}$$

The value for FeH alloy is taken to be

$$10^3\ln(\beta_{FeH}) = \frac{4{,}281.4(2.597P(\text{GPa}) + 119.017)}{T^2}. \tag{33}$$

The fractionation factor, expressed as $10^3\ln(\alpha_{silicate-FeH}) \approx \delta^{57}Fe_{silicate} - \delta^{57}Fe_{FeH}$ is then

$$10^3\ln(\alpha_{silicate-FeH}) = 10^3\ln(\beta_{Fe-silicate}) - 10^3\ln(\beta_{FeH}). \tag{34}$$

We used the FeH alloy for the entire metal as the mole fractions of H in our Fe metal phases are high (about 0.27), and the effect of different Fe/H ratios on the fractionation factors are not yet understood.

To evaluate the Si isotope effects, we used the $^{30}Si/^{28}Si$ fractionation determined both by experiments and by analysis of equilibrated aubrites[75], yielding

$$10^3\ln(\alpha_{silicate-metal}) = \frac{7.64 \times 10^6}{T^2}. \tag{35}$$

Similar to the Fe isotope effects described in the main text, our model predicts that the $^{30}Si/^{28}Si$ ratio of the bulk silicates (expressed as $\delta^{30}Si$) should be greater than the source material by 0.06‰. This offset is smaller than the observed difference between Earth and many chondrites of about 0.2‰ (ref. [79]) and is much smaller than the difference between Earth and E chondrites[80], despite the similarity between Earth and E chondrites in virtually every other isotope system. Our results do not alleviate some of the vexing aspects of Si isotope variability in the Solar System. In general, the apparently anomalous Si isotopic composition of E chondrites may be related to the apparent excess in Si in these rocks (about 20% atomic) compared with solar refractory metal abundances.

The deuterium/hydrogen (D/H) of the Sun ($D/H = 2.0 \times 10^{-5}$), and thus the protosolar gas, expressed as δD relative to ocean water ($D/H = 1.558 \times 10^{-4}$), is about −865‰ (ref. [81]). Recent estimates for the bulk D/H ratio of Earth's H yield a value for δD relative to ocean water of −218‰ (ref. [76]). It is conventional to ascribe the origin of Earth's water to late addition of small bodies, asteroids or comets, because

virtually all sources of D/H in the Solar System other than protosolar gas, including comets[82,83], chondrite meteorites[84] and water in icy moons[85], have $\delta D \geq 0$, and often much greater than 0 (Extended Data Fig. 5). Calculations based on mixing of asteroids and/or comets with a solar gas based on D/H ratios suggest that there may be a solar-gas component comprising roughly 25% to 40% of H deep within the Earth, depending on whether the non-solar component is chondrite-like or comet-like. For comparison, $^{20}Ne/^{22}Ne$ data suggest Earth acquired about two-thirds of its neon from the solar gas and the remaining one-third from E chondrite-like material[26].

In general, any reactions between H_2 and H_2O, either at equilibrium or kinetically controlled through reactive intermediates, result in D/H of H_2O being greater than that of H_2, so the use of D/H as a tracer involves numerous degeneracies. At room temperature and below, the kinetic or equilibrium preferential transfer of D to H_2O from solar-like H_2 will result in D/H in H_2O comparable to or greater than those observed in Solar System H_2O. Therefore, it is likely that a variety of different processes were at work to cause the generally high D/H of H_2O in the Solar System.

Motivated by the model presented here, we consider the possibility that the high D/H of Earth's H_2O and deep interior could be the residual effect of low-temperature exchange of D and H between H_2O and H_2 in embryo atmospheres, and the sequestration of large fractions of H in the metallic cores. The convecting silicate magma oceans would serve as the conveyor linking the atmospheres and metal cores in this context. Hydrogen isotope exchange between radical derivatives of H_2 gas and water at temperatures similar to the equilibrium temperature at the top of an embryo atmosphere at about 1 AU (255 K present day, 237 K accounting for a fainter Sun 4.6 Gyr before present[86]) will result in high D/H in the atmosphere[87] if there is a balancing sink for the low-D/H complement of H. In the model of ref. [87], higher D/H in atmospheric H_2O is balanced by slow (over billion-year timescales) hydrodynamic escape of isotopically light H[88]. Another study[27] also advanced the idea that the high D/H of Earth's H_2O was due to hydrodynamic escape, in this case as H rather than H_2. In our model, the requisite low-D/H sinks for H that balance the high D/H of terrestrial water are the metal cores; H isotope equilibration between embryo metal cores, silicate mantles and atmospheres results in a high-D/H atmospheres and low-D/H metal cores.

This explanation relies on a faster rate of isotope exchange high in the atmosphere where temperatures are low (<300 K) than exchange at high temperatures near the surface of the magma ocean. A detailed atmospheric model is beyond the scope of the present study, but we note that D/H exchange is expected to be orders of magnitude faster in the upper atmosphere where kinetics mediated by radicals result from low densities and photochemistry compared with exchange between H_2O and H_2 molecules at high temperatures and densities. For example, the forward rate constant for the reaction HD + OH → HDO + H at a temperature of 237 K (representing the 1-AU equilibrium temperature for the stratosphere of an embryo 4.5 Gyr before present) is 1.9×10^{-15} cm^3 s^{-1} (ref. [89]). This reaction represents transfer of D from H to OH, and ultimately H_2O, in embryo stratospheres. The rate constant for the reaction H_2 + HDO → HD + H_2O is 1.4×10^{-23} cm^3 s^{-1} at 1,973 K, the latter temperature being an altitude-averaged temperature for the adiabatic tropospheres of atmospheres implied by our models. This represents return of D from H_2O to H in the tropospheres. Although the details rely on a number of uncertain parameters, including ratios of e-folding times for exchange and residence times in the various reservoirs, it is unlikely that this disparity in rate constants can be overcome by the relative masses of H_2O and H_2 in the embryo stratospheres and tropospheres (for reference, Earth's ratio of moles in the stratosphere to moles in the troposphere is 0.1)[90]. Vigorous mixing of H_2O and H between the stratosphere and troposphere should therefore result in D/H isotope fractionation dominated by the lower temperatures. The turnover time for Earth's stratosphere is about 2.5 years due to transfer back and forth between the stratosphere and troposphere[90]. We speculate that it is likely that H_2 and the underlying magma oceans could have reached isotopic equilibrium during the earliest phases of dissolving molecular hydrogen into the melts[91].

As a plausibility exercise based on the reasoning described above, we calculated the relative abundances of the deuterated species in the stratospheres and tropospheres from the surface densities (column densities) of an adiabatic troposphere at the surface of the magma ocean and the surface density of the stratosphere as measured at the tropopause using a simplified atmosphere[22]. The mixing ratio of H_2O was taken to be 0.8 with the remainder of the atmosphere being H_2. The temperature at the base of the troposphere was taken to be the potential temperature of the magma oceans in our model (2,350 K), the height of the tropopause was assumed to be where the temperature reaches the equilibrium temperature and the stratosphere was taken to be isothermal, extending five surface-scale heights. From this, we obtain a ratio of moles of HD in the stratosphere to moles of HDO in the troposphere, N_{HD}/N_{HDO}, of 3×10^{-4}. Converting the rate constants for the two reactions described above to k(mol^{-1} yr^{-1}) using k(cm^3 s^{-1})L/V, where L is Avogadro's number and V are the similar volumes of each of the two reservoirs, one obtains rate constants of 4.3×10^{-10} mol^{-1} yr^{-1} for HD + OH → HDO + H at a temperature of 237 K and 1.1×10^{-18} mol^{-1} yr^{-1} for H_2 + HDO → HD + H_2O at 1,973 K. From these values, one obtains a time constant for D/H exchange in the stratosphere of 5×10^{-7} yr for an OH/H_2O ratio of about 10^{-4} and a time constant for D/H exchange in the troposphere of 1×10^{-4} yr. Smaller concentrations of OH result in proportionally larger time constants in the stratosphere; equal time constants for exchange in the stratosphere and troposphere would require OH/H_2O ratios of about 10^{-7}.

We take the shorter time constant for D/H exchange in the stratosphere relative to the troposphere to mean that a low-temperature for H_2O–H_2 D/H exchange in the atmosphere on average is plausible. Equilibrium D/H exchange between H_2O and H_2 has been inferred for the Martian atmosphere at similar temperatures of about 200 K (ref. [92]). We note for comparison that various terrestrial analogues exist for isotopic anomalies formed in the stratosphere to persist in the troposphere, including in the cases of oxygen and nitrogen isotopologues[93,94].

Here we adopted a low temperature of exchange between atmospheric H_2O and H_2 and calculated the equilibrium δD values associated with our model relative to the primordial hydrogen atmospheres of embryos. Our calculations assume H isotopic equilibrium between atmospheres, magma oceans and molten metal cores. We obtained δD values for atmospheric H_2, atmospheric H_2O, H in silicate melt and H in metal at equilibrium by solving the H isotope mass-balance equation $\delta D(\text{bulk}) = \sum_i x_{H,i}\,\delta D_i$, where $x_{H,i}$ refers to the H fraction for each phase i, together with the equilibrium differences between reservoirs i and j of the form $\delta D_i - \delta D_j = 10^3 \ln(\alpha_{i-j})$ for the high-T fractionations, and $\delta D_{H_2O} - \alpha_{H_2O-H_2}\delta D_{H_2} = 10^3(\alpha_{H_2O-H_2} - 1)$ for the lower-T, and thus much larger, atmospheric H_2O and H_2 fractionation. We thus have four equations for four unknown δD values given three known fractionation factors, α, and an assigned value for δD (system) (taken to be 0 for reference). The equations to be solved, in matrix form, are

$$\begin{bmatrix} x_{H,H_2} & x_{H,H_2O} & x_{H,sil} & x_{H,metal} \\ 0 & 0 & 1 & -1 \\ -\alpha_{H_2O-H_2} & 1 & 0 & 0 \\ -1 & 0 & 1 & 0 \end{bmatrix} \begin{bmatrix} \delta D_{H_2} \\ \delta D_{H_2O} \\ \delta D_{sil} \\ \delta D_{metal} \end{bmatrix} = \begin{bmatrix} \delta D_{system} = 0 \\ 10^3 \ln(\alpha_{slicate-metal}) \\ 10^3(\alpha_{H_2O-H_2} - 1) \\ 10^3 \ln(\alpha_{silicate-H_2}) \end{bmatrix} \quad (36)$$

We used fractionation factors described previously by ref. [75]. The fractionation factors for D/H, expressed as per mil differences in δD values, or $10^3 \ln(\alpha)$, include the value for silicate and metal (that is, $\delta D_{silicate} - \delta D_{metal}$):

$$10^3 \ln(\alpha_{silicate-metal}) = \frac{4.5 \times 10^8}{T^2_{core-mantle}}, \quad (37)$$

the value for H_2O and H_2:

$$10^3 \ln(\alpha_{H_2O-H_2}) = \frac{215.8 \times 10^3}{T_{atmosphere}}, \quad (38)$$

and the value between silicate and H_2 gas based on the difference between $10^3 \ln(\alpha_{silicate-metal})$ and the fractionation between H_2 and metal[75]:

$$10^3 \ln(\alpha_{silicate-H_2}) = \frac{4.5 \times 10^8}{T^2_{surface}} - \frac{3.261 \times 10^8}{T^2_{surface}}. \quad (39)$$

Each equilibrium is specified to occur at the core–mantle boundary, in the atmosphere or at the atmosphere–magma ocean interface at the specified temperatures of 3,000 K, 237 K and 2,350 K, respectively. The results are shown in Extended Data Fig. 5. If the structure of the atmospheres of the embryos was such that D/H exchange in the atmosphere was dominated by lower temperatures, the D/H of terrestrial H_2O is explained by our model. The implied D/H of the primordial atmosphere source is similar to that for Uranus and Neptune and greater than the solar value (Extended Data Fig. 5), allowing for some late additions of H_2O to Earth by high-D/H bolides. We emphasize that this model is possible because of the metal cores serving as low-D/H reservoirs.

Data availability

Example model results are available as Supplementary tables.

Code availability

The Python code used for the models shown in Fig. 1 in this study is available at GitHub: https://github.com/eyoungucla/chems/blob/main/Exoplanet_atmosphere_model_vMCMC_coreT_3000K_dist.py.

57. Corgne, A., Keshav, S., Wood, B. J., McDonough, W. F. & Fei, Y. Metal–silicate partitioning and constraints on core composition and oxygen fugacity during Earth accretion. *Geochim. Cosmochim. Acta* **72**, 574–589 (2008).
58. Fegley, J. B. & Cameran, A. G. W. A vaporization model for iron/silicate fractionation in the Mercury protoplanet. *Earth Planet. Sci. Lett.* **82**, 207–222 (1987).
59. Schaefer, L. & Fegley, B. Chemistry of silicate atmospheres of evaporating super-Earths. *Astrophys. J.* **703**, L113–L117 (2009).
60. Hastie, J. & Bonnell, D. A predictive thermodynamic model of oxide and halide glass phase equilibria. *J. Non Crystalline Solids* **84**, 151–158 (1986).
61. Xiang, Y., Sun, D., Fan, W. & Gong, X. Generalized simulated annealing algorithm and its application to the thomson model. *Phys. Lett. A* **233**, 216–220 (1997).
62. Foreman-Mackey, D. et al. emcee v3: a Python ensemble sampling toolkit for affine-invariant MCMC. *J. Open Source Softw.* **14**, 1864 (2019).
63. Goodman, J. & Weare, J. Ensemble samplers with affine invariance. *Commun. Appl. Math. Comput. Sci.* **5**, 65–80 (2010).
64. Kovačević, T., González-Cataldo, F., Stewart, S. T. & Militzer, B. Miscibility of rock and ice in the interiors of water worlds. *Sci. Rep.* **12**, 13055 (2022).
65. Xiao, B. & Stixrude, L. Critical vaporization of $MgSiO_3$. *Proc. Natl Acad. Sci. USA* **115**, 5371–5376 (2018).
66. Boorstein, W. M. & Pehlke, R. D. Measurement of hydrogen solubility in liquid iron alloys employing a constant volume technique. *Metall. Mater. Trans. B* **5**, 399–405 (1974).
67. Waseda, Y. Interaction parameters in metallic solutions estimated from liquid structure and the heat of solution at infinite dilution. *High Temp. Mater. Processes* **31**, 203–208 (2012).
68. Righter, K., Rowland, R.II, Yang, S. & Humayun, M. Activity coefficients of siderophile elements in Fe–Si liquids at high pressure. *Geochem. Persp. Lett.* **15**, 44–49 (2020).
69. Hirschmann, M., Withers, A., Ardia, P. & Foley, N. Solubility of molecular hydrogen in silicate melts and consequences for volatile evolution of terrestrial planets. *Earth Planet. Sci. Lett.***345**, 38–48 (2012).
70. Okuchi, T. Hydrogen partitioning into molten iron at high pressure: implications for Earth's core. *Science* **278**, 1781–1784 (1997).
71. Moore, G., Vennemann, T. & Carmichael, I. An empirical model for the solubility of H_2O in magmas to 3 kilobars. *Am. Mineral.* **83**, 36–42 (1998).
72. Karki, B. B., Wentzcovitch, R. M., de Gironcoli, S. & Baroni, S. Ab initio lattice dynamics of $MgSiO_3$ perovskite at high pressure. *Phys. Rev. B* **62**, 14750–14756 (2000).
73. Katsura, T. et al. Thermal expansion of forsterite at high pressures determined by in situ X-ray diffraction: the adiabatic geotherm in the upper mantle. *Phys. Earth Planet. Inter.* **174**, 86–92 (2009).
74. Shahar, A. & Young, E. D. An assessment of iron isotope fractionation during core formation. *Chem. Geol.* **554**, 119800 (2020).
75. Young, E. D. et al. High-temperature equilibrium isotope fractionation of non-traditional stable isotopes: experiments, theory, and applications. *Chem. Geol.* **395**, 176–195 (2015).
76. Hallis, L. J. et al. Evidence for primordial water in Earth's deep mantle. *Science* **350**, 795–797 (2015).
77. Sossi, P. A., Nebel, O. & Foden, J. Iron isotope systematics in planetary reservoirs. *Earth Planet. Sci. Lett.* **452**, 295–308 (2016).
78. Ni, P. et al. Planet size controls Fe isotope fractionation between mantle and core. *Geophys. Res. Lett.* **49**, e2022GL098451 (2022).
79. Pringle, E. A., Moynier, F., Savage, P. S., Badro, J. & Barrat, J.-A. Silicon isotopes in angrites and volatile loss in planetesimals. *Proc. Natl Acad. Sci. USA* **111**, 17029–17032 (2014).
80. Savage, P. S. & Moynier, F. Silicon isotopic variation in enstatite meteorites: clues to their origin and Earth-forming material. *Earth Planet. Sci. Lett.* **361**, 487–496 (2013).
81. Geiss, J. & Gloeckler, G. Isotopic composition of H, He and Ne in the protosolar cloud. *Space Sci. Rev.* **106**, 3–18 (2003).
82. Altwegg, K. et al. 67P/Churyumov–Gerasimenko, a Jupiter family comet with a high D/H ratio. *Science* **347**, 1261952 (2015).
83. Bockelée-Morvan, D. et al. Herschel measurements of the D/H and $^{16}O/^{18}O$ ratios in water in the Oort-cloud comet C/2009P1 (Garradd). *Astron. Astrophys.* **544**, L15 (2012).
84. Alexander, C. M. O. et al. The provenances of asteroids, and their contributions to the volatile inventories of the terrestrial planets. *Science* **337**, 721–723 (2012).
85. Waite Jr, J. H. et al. Liquid water on Enceladus from observations of ammonia and ^{40}Ar in the plume. *Nature* **460**, 487–490 (2009).
86. Gough, D. O. Solar interior structure and luminosity variations. *Solar Phys.* **74**, 21–34 (1981).
87. Genda, H. & Ikoma, M. Origin of the ocean on the Earth: early evolution of water D/H in a hydrogen-rich atmosphere. *Icarus* **194**, 42–52 (2008).
88. Lammer, H. et al. Origin and loss of nebula-captured hydrogen envelopes from 'sub'- to 'super-Earths' in the habitable zone of Sun-like stars. *Mon. Not. R. Astron. Soc.* **439**, 3225–3238 (2014).
89. Yang, L., Ciesla, F. J. & Alexander, C. M. The D/H ratio of water in the solar nebula during its formation and evolution. *Icarus* **226**, 256–267 (2013).
90. Holton, J. R. On the global exchange of mass between the stratosphere and troposphere. *J. Atmos. Sci.* **47**, 392–395 (1990).
91. Pahlevan, K., Schaefer, L. & Hirschmann, M. M. Hydrogen isotopic evidence for early oxidation of silicate Earth. *Earth Planet. Sci. Lett.* **526**, 115770 (2019).
92. Krasnopolsky, V. A., Mumma, M. J. & Gladstone, G. R. Detection of atomic deuterium in the upper atmosphere of Mars. *Science* **280**, 1576–1580 (1998).
93. Young, E., Yeung, L. & Kohl, I. On the $\Delta^{17}O$ budget of atmospheric O_2. *Geochim. Cosmochim. Acta* **135**, 102–125 (2014).
94. Yeung, L. Y. et al. Extreme enrichment in atmospheric $^{15}N^{15}N$. *Sci. Adv.* **3**, eaao6741 (2017).
95. Barnes, J. J. et al. The origin of water in the primitive Moon as revealed by the lunar highlands samples. *Earth Planet. Sci. Lett.* **390**, 244–252 (2014).
96. Lellouch, E. et al. The deuterium abundance in Jupiter And Saturn from ISO-SWS observations. *Astron. Astrophys.* **670**, 610–622 (2001).
97. Feuchtgruber, H. et al. The D/H ratio in the atmospheres of Uranus and Neptune from Herschel-PACS observations. *Astron. Astrophys.* **551**, A126 (2013).

Acknowledgements This AEThER publication is funded in part by the Alfred P. Sloan Foundation under grant G202114194. H.E.S. gratefully acknowledges NASA grant 80NSSC18K0828 for financial support during preparation and submission of the work.

Author contributions All authors contributed significantly to the formal analysis. E.D.Y. led the writing of the paper aided by A.S. and H.E.S.

Competing interests The authors declare no competing interests.

Additional information

Supplementary information The online version contains supplementary material available at https://doi.org/10.1038/s41586-023-05823-0.

Correspondence and requests for materials should be addressed to Edward D. Young.

Peer review information *Nature* thanks David Catling and the other, anonymous, reviewer(s) for their contribution to the peer review of this work. Peer reviewer reports are available.

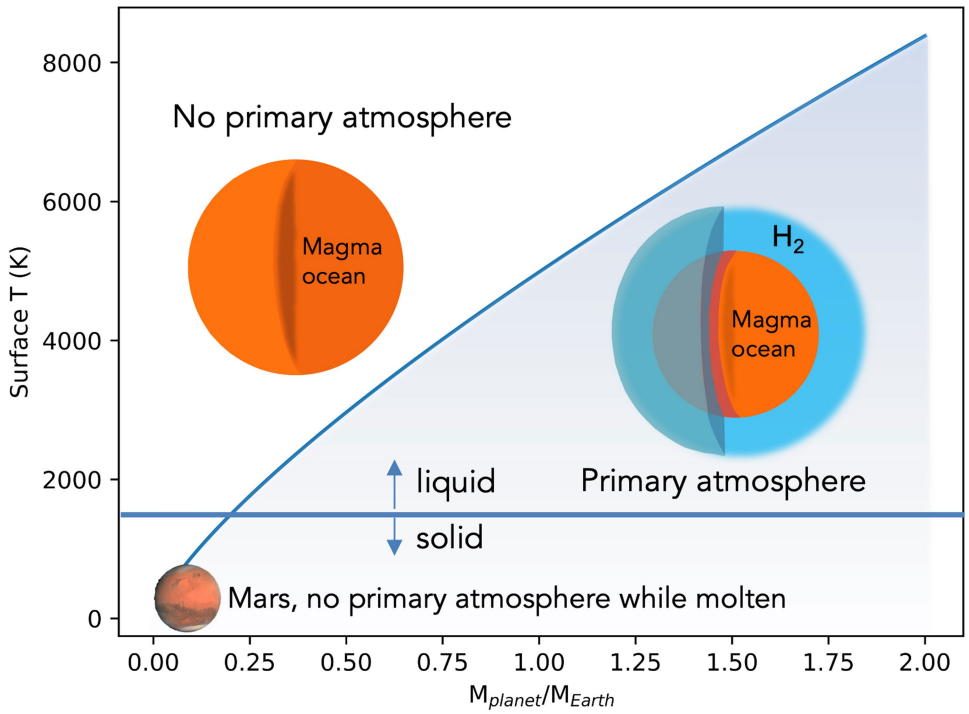

Extended Data Fig. 1 | Plot of surface temperatures that allow for a gravitationally bound primary H_2 atmosphere versus mass of planetary embryos[19]. The region in temperature-mass space where a primary atmosphere is possible is shaded. The approximate solidus for silicate melt is overlain as the horizontal line.

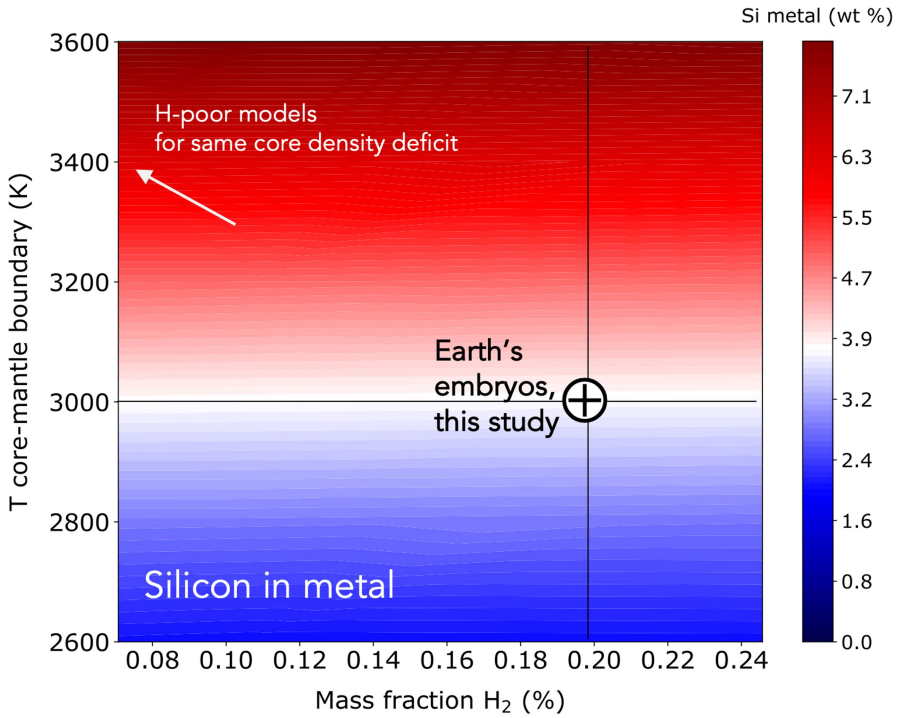

Extended Data Fig. 2 | Summary of equilibrium calculations for Si in metal in embryos with masses of 0.5$M_\oplus$ as a function of metal–silicate equilibration temperature ($T_{core-mantle}$) and mass fraction of initial primary H_2-rich atmosphere relative to the planet. Arrow illustrates values for models that satisfy the required density deficit in the core but where H is scarce or absent.

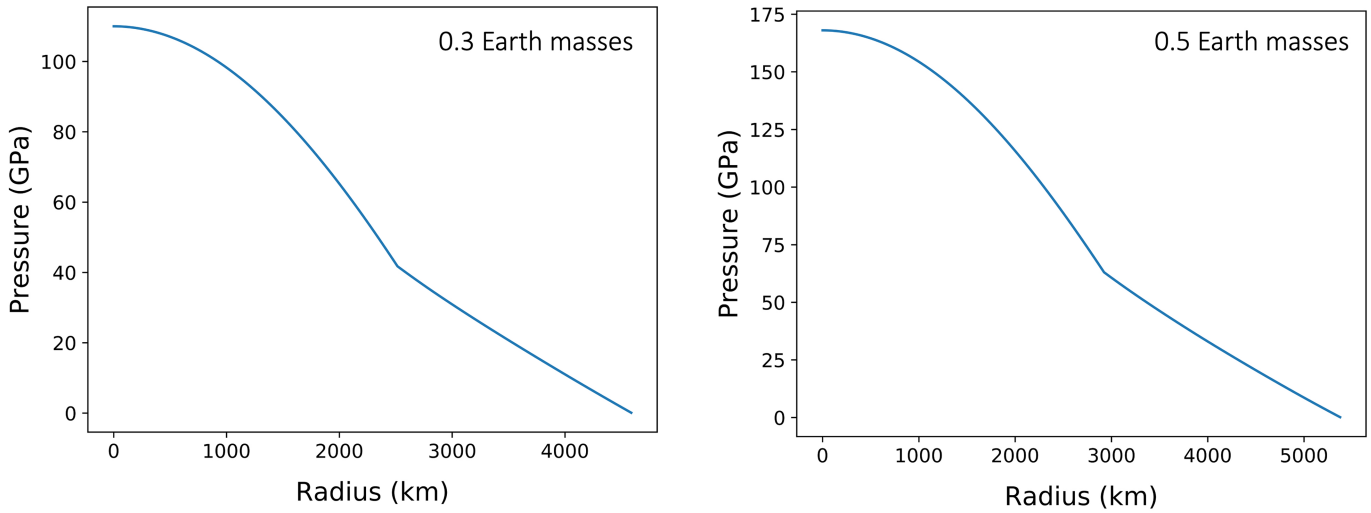

Extended Data Fig. 3 | Pressure vs. radius for $0.3M_{\oplus}$ (left) and $0.5M_{\oplus}$ (right) embryos. Breaks in slope mark the core–mantle boundaries.

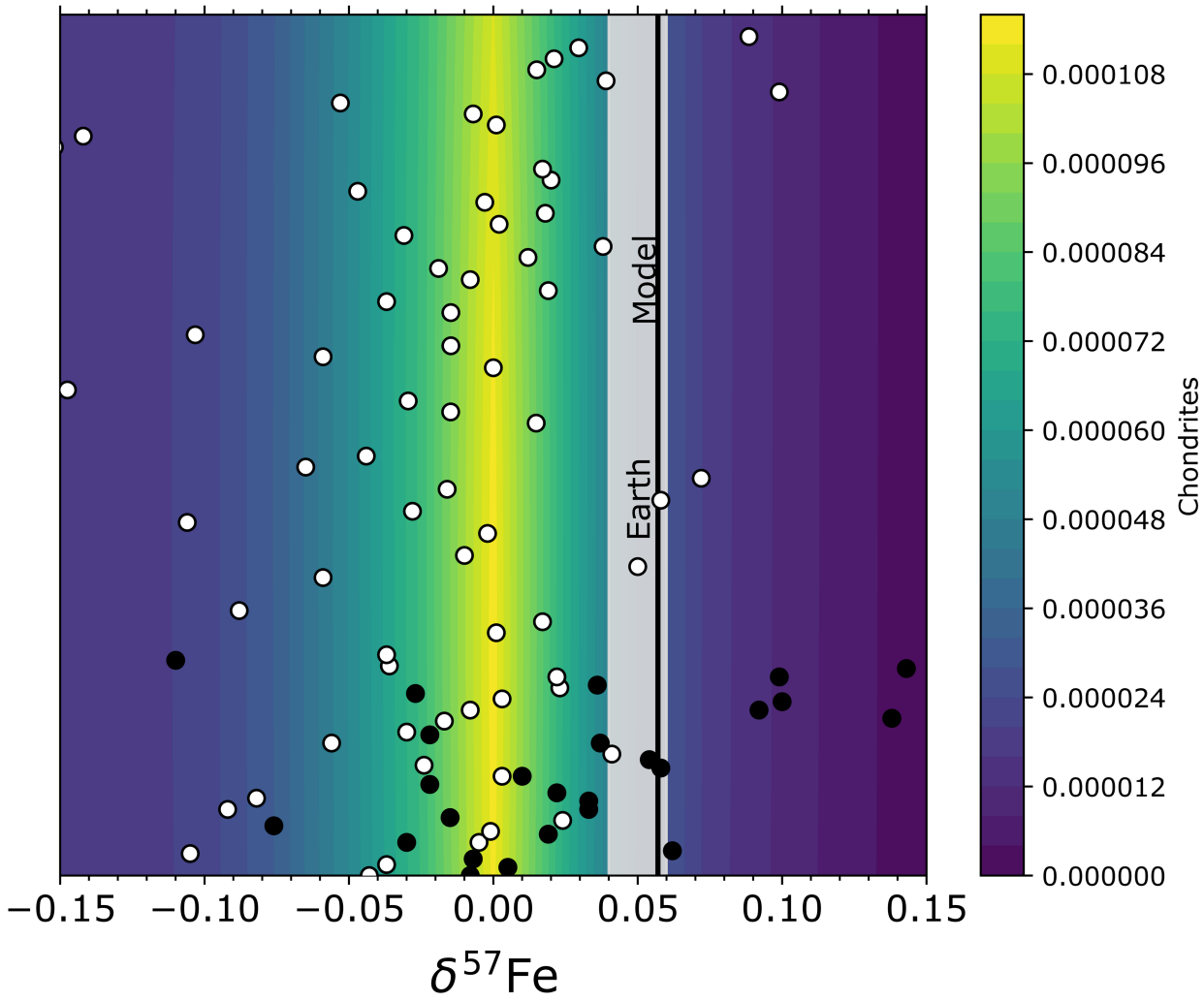

Extended Data Fig. 4 | Iron isotope ratios of bulk silicate for model embryos compared with recent estimates for bulk Earth (grey bar) and chondrites showing that the model reproduces the offset between initial materials (chondrites, δ^{57}Fe = 0) and Earth. Black filled symbols are for E chondrites while white symbols are for all other chondrite groups. The multi-colour contours are probability densities for the chondrite δ^{57}Fe values with an average indistinguishable from δ^{57}Fe = 0.0. The y axis values are assigned randomly to each datum in equal spacings for clarity, with E chondrites confined to the lower quarter of the ordinate.

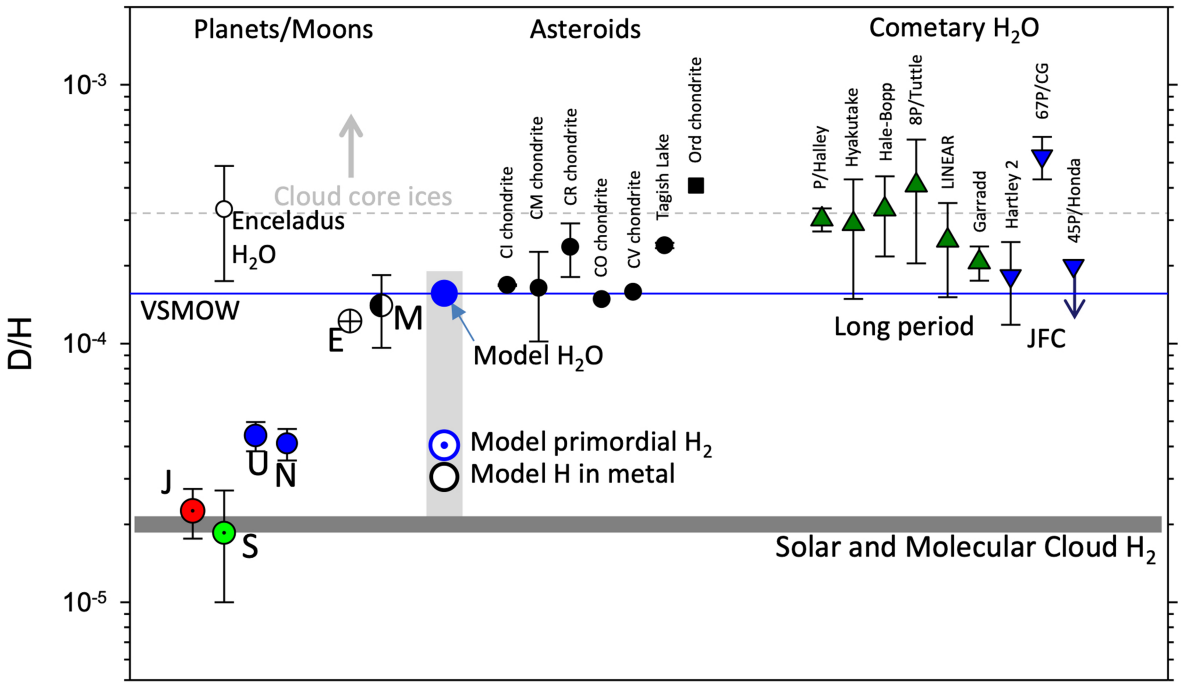

Extended Data Fig. 5 | Summary of D/H ratios for Solar System materials from a variety of literature sources. The circle + symbol labelled E denotes bulk Earth[76]. Black/white symbol labelled M refers to lunar highland apatites[95]. Blue symbols refer to calculated values for original water based on measured asteroidal rock values[84]. U, N, J, and S refer to Uranus, Neptune, Jupiter, and Saturn, respectively[96,97]. Model values for Earth's water, primordial hydrogen atmosphere, and metal described here are indicated within the grey box, where the model is assigned the terrestrial value.